Article

Constitutive Equation and Hot Processing Map of Mg-16Al Magnesium Alloy Bars

Zongwen Ma [1] [iD], Fengya Hu [2], Zhongjun Wang [1],*, Kuijun Fu [2], Zhenxiong Wei [1], Jiaji Wang [2] and Weijuan Li [1]

[1] School of Materials and Metallurgy, University of Science and Technology Liaoning, Anshan 114051, China; ustlmzw@gmail.com (Z.M.); zhenxiongwei111@gmail.com (Z.W.); ustllwj@gmail.com (W.L.)

[2] State Key Laboratory of Metal Material for Marine Equipment and Application, Ansteel Group Corporation, Anshan 114009, China; aghfy312@gmail.com (F.H.); agfkj63@gmail.com (K.F.); agwjj2013@gmail.com (J.W.)

* Correspondence: ustlwzj@gmail.com; Tel.: +86-412-59-29926

Abstract: A Gleeble-2000D thermal simulation machine was used to investigate the high-temperature hot compression deformation of an extruded Mg-16Al magnesium alloy under various strain rates (0.0001–0.1 s^{-1}) and temperatures (523–673 K). Combined with the strain compensation Arrhenius equation and the Zener–Hollomon (Z) parameter, the constitutive equation of the alloy was constructed. The average deformation activation energy, Q, was 144 KJ/mol, and the strain hardening index ($n \approx 3$) under different strain variables indicated that the thermal deformation mechanism was controlled by dislocation slip. The Mg-16Al alloy predicted by the Sellars model was characterized by a small dynamic recrystallization (DRX) critical strain, indicating that $Mg_{17}Al_{12}$ particles precipitated during the compression deformation promoted the nucleation of DRX. Hot processing maps of the alloy were established based on the dynamic material model. These maps indicated that the high Al content, precipitation of numerous $Mg_{17}Al_{12}$ phases, and generation of microcracks at low temperature and low strain rate led to an unstable flow of the alloy. The range of suitable hot working parameters of the experimental alloy was relatively small, i.e., the temperature range was 633–673 K, and the strain rate range was 0.001–0.1 s^{-1}.

Keywords: magnesium alloy; Mg-16Al; hot deformation; constitutive equation; processing maps

1. Introduction

Magnesium (Mg) alloys are characterized by excellent specific strength, specific stiffness, electromagnetic shielding, damping, and other characteristics, and they have good application prospects in many fields (e.g., automobiles, electronic communications, and aerospace) [1–3]. The unique close-packed hexagonal crystal structure of Mg alloys and the limited sliding system at ambient temperature limit the workability and, hence, industrial application of these alloys [4]. Therefore, optimizing the thermal processing parameters and mastering the thermal deformation characteristics of Mg alloys are essential for controlling the structural evolution and mechanical properties of these materials. A thermal processing map based on the dynamic material model (DMM) combined with the microstructure of the material is used to optimize the thermal processing parameters of the material. For Mg-Al alloys, adding the Al element to Mg is effective in improving the yield strength and casting performance of a Mg alloy. The work of Prasad et al. [5] suggested that homogenization treatment is beneficial for expanding the processable area of cast AZ31 Mg alloy and leads to a significant reduction in the number of intergranular cracks and area of rheological instability. Wei et al. [6] discussed the hot tensile deformation characteristics and obtained the hot working map of an aged and homogenized AZ61Ce Mg alloy sheet. The results indicated that the aging treatment and homogenization treatment

were beneficial for expanding the workable area of the alloy. Lou et al. [7] found that the processing map of extruded AZ80 Mg alloy in the stretched state consisted of two dynamic recrystallization (DRX) regions with small equiaxed crystals. Xu et al. [8] reported that the DRX tissue region of AZ91D exhibited good thermal processing performance, and this region was taken as the processable region for AZ91D thermal processing.

The occurrence of DRX will generally promote grain refinement and reduce the flow stress, thereby helping to improve the formability of materials. Furthermore, the relatively low stacking fault energy (SF) and high grain boundary diffusion rate of Mg alloy are beneficial to the occurrence of DRX [9]. Poliak and Jonas [10] proposed that an inflection point will occur in the strain hardening rate (θ) and stress (σ) curves of materials undergoing DRX. Poliak et al. [10–13] used a second derivative method to predict the critical strain (ε_c) of DRX. The Sellars model [14] is a prediction model based on the Poliak–Jonas criterion, where the influence of temperature (T) and strain rate ($\dot{\varepsilon}$) is considered, and the Zener–Hollomon (Z) parameter is used to obtain the ε_c of DRX. The Sellars models of Mg-11.95Gd-4.5Y-2Zn-0.37Zr, AZ80, and AZ61 alloys were established by Yu [15], Su [16], and Wei [17], respectively.

The Arrhenius-type constitutive equation has been widely used to describe the changing characteristics of flow stress and deformation temperature and strain rate [18–21]. However, only a few reports have considered the high temperature plastic deformation behavior of deformed Mg alloys with high Al content. Therefore, in the present work, the hot compression deformation characteristics of Mg-16Al Mg alloy hot extruded bars were investigated, and the corresponding constitutive equation and hot processing map were established. The optimal hot working parameter range of the alloy was determined, which provided a basis for optimizing the development of Mg alloys with high Al content.

2. Materials and Methods

A semi-continuously cast Mg alloy bar with a diameter of 135 mm was cold-cut and peeled to a diameter of 120 mm. This bar was then hot-extruded at 673 K into a 45 mm–diameter bar, which was taken as the experimental material. After hot extrusion, the material was left to cool in the air. The nominal chemical composition of the material was 16 wt.% Al, 0.2 wt.% Zn, 0.3 wt.% Mn, 0.4 wt.% Ce, 0.2 wt.% Sr, and balance Mg. Prior to hot compression deformation, the experimental alloy was solution-treated at a temperature of 673 K for 12 h. As shown in Figure 1, the hot compression sample was taken at a position 0.6 R away from the axial center of the test bar and processed into a $\Phi 12.0 \times 18.0$ mm cylinder.
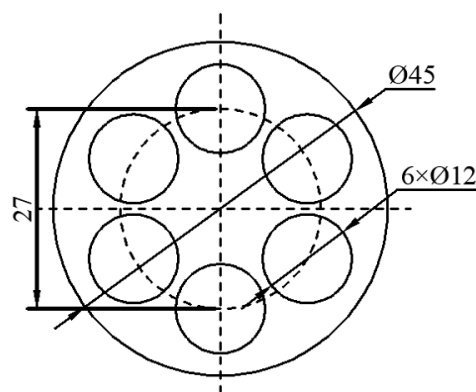

Figure 1. Sampling location of hot compressed specimens.

The specimens after solution treatment were subjected to a thermal compression test on a Gleeble-2000D thermal simulation test machine (Data Sciences International, DE, USA), where the compression axis was set parallel to the existing extrusion direction. Temperatures of 523, 573, 623, and 673 K, and strain rates of 0.0001, 0.001, 0.01, and 0.1 s^{-1}, respectively (maximum engineering strain:

80%), were employed during the experiment. A small amount of lubricating oil was inserted between the indenter and the specimen, to reduce the friction between these components. Each specimen was heated to the set temperature, held for 3 min, and then subjected to the hot compression test. After testing, the specimen was immediately cooled in water, to retain the structural characteristics after thermal deformation.

The microstructure of the Mg-16Al Mg alloy was examined via metallographic observations. For this examination, the specimens after hot compression deformation were cut along the direction parallel to the compression axis, and the section microstructures were observed. The specimens were polished and etched for optical microscopy (OM) observation. An etchant (1 mL water, 1 mL glacial acetic acid, 10 mL absolute ethanol, and 0.5 g picric acid solution) was used in the preparation of the samples. Cotton was dipped into the solution, which was then lightly smeared in one direction along the polished surface of the specimen. After a certain corrosion time, the surface was wiped with cotton, washed with water, and then washed with alcohol, to remove any residual corrosive solution. After drying, the microstructures of the specimens were observed under an optical microscope, and the fine microstructures were observed by scanning electron microscope (SEM, Zeiss-ΣIGMA HD, Thuringia, Germany) equipped with energy dispersive spectrometer (EDS).

3. Results and Discussion

3.1. The Original Microstructure of Mg-16Al before Deformation

The specimens subjected to a hot extrusion and solution treatment (673 K, 12 h) were observed via SEM. As shown in Figure 2a, the original hot extrusion microstructure was mainly composed of matrix α-Mg grains, β-$Mg_{17}Al_{12}$ phases with discontinuous reticular distribution near the α-Mg grains boundaries (GBs), and γ-$Mg_{17}Al_{12}$ phases with a cellular structure inside the α-Mg grains. Moreover, unevenly distributed Ce-containing rare-earth phases were also present in the hot extrusion specimens. The γ-$Mg_{17}Al_{12}$ (i.e., a cellular phase, as previously stated) is shown in Figure 3. Figure 2b shows the microstructure after the solution treatment. The massive α-Mg grains in the specimens are considerably larger than those in the hot-extruded specimens. Coarse β-$Mg_{17}Al_{12}$ phases at the GBs were only partly dissolved in the matrix, owing to the large number of Al atoms in the experimental alloy. Due to the solution treatment, the previously discontinuous reticular β-$Mg_{17}Al_{12}$ phases were partially dissolved, whereas the γ-$Mg_{17}Al_{12}$ phases were completely dissolved in the α-Mg matrix. Similarly, Al-atom diffusion into the matrix accompanied by grain boundary migration led eventually to an increase in the size of the α-Mg grains (average size increased from 10 to 25 μm).
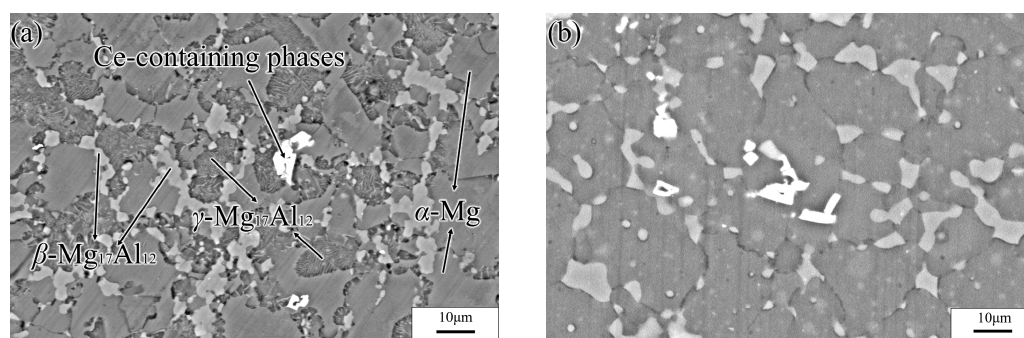

Figure 2. SEM images of Mg-16Al Mg alloy before (**a**) and after (**b**) solution treatment with 400 °C holding for 12 h.
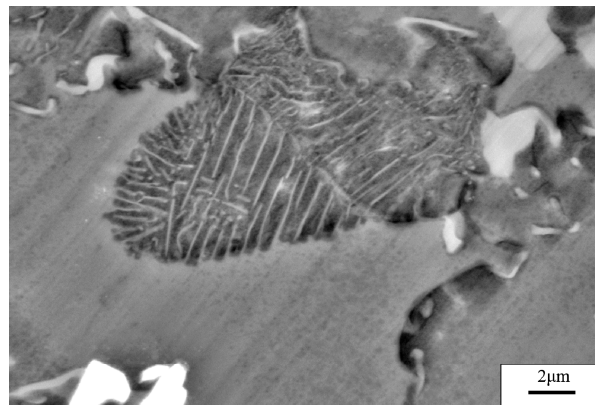
Figure 3. SEM image of the γ-Mg$_{17}$Al$_{12}$ phase.

3.2. The Microstructure of Mg-16Al after Deformation

Figure 4a shows a SEM image of the experimental alloy after deformation at low temperature and strain rate (523 K/0.0001 s^{-1}). The microstructure consisted of many uniformly distributed recrystallized grains (average grain size: 15 μm). Numerous Al atoms diffused into the α-Mg grains, and, hence, many γ-Mg$_{17}$Al$_{12}$ phases were continuously precipitated in the final grains. Moreover, discontinuously distributed β-Mg$_{17}$Al$_{12}$ phase particles were present at the GBs. Figure 4b shows an SEM image of the experimental alloy after deformation at high temperature and strain rate (673 K/0.1 s^{-1}). The alloy underwent DRX, which yielded an average grain size of 10 μm. The discontinuously distributed β-Mg$_{17}$Al$_{12}$ phase particles at the GBs were stretched along the direction rotated 45° with respect to the compression axis. Similarly, a small number of Mg$_{17}$Al$_{12}$ phases were discontinuously precipitated from the α-Mg matrix at the GBs.
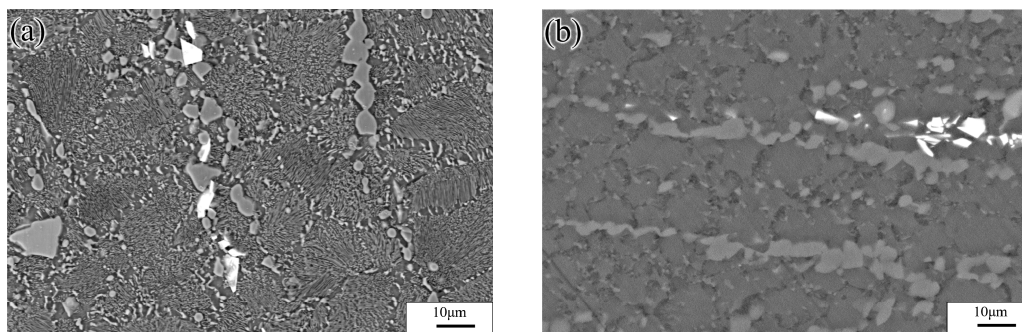

Figure 4. SEM images of experimental alloy deformed under different conditions: (**a**) 523 K/0.0001 s^{-1} and (**b**) 673 K/0.1 s^{-1}.

3.3. Flow Behavior

The stress–strain curves of the experimental alloy specimens after solution treatment at various deformation conditions are shown in Figure 5. Obviously, the flow stress was affected by temperature and strain rate, and the peak stress and steady-state stress both increased with decreasing temperature and increasing strain rate. The stress–strain curves all exhibited significant recrystallization characteristics and a consistent variation trend: The flow stress increased sharply with increasing true strain, and then the rate of increase decreased gradually. The stress decreased gradually after reaching a peak value. When the deformation reached a certain true strain, the stress value remained basically unchanged. Moreover, the work hardening rate and flow softening rate varied with the strain rate and deformation temperature. At relatively high strain rate levels ($\dot{\varepsilon} \geq 0.01$ s^{-1}), considerable work hardening and subsequent continuous flow softening were observed, but a significantly different flow behavior was observed at lower strain rates. At relatively high temperatures (T $\geq$ 623 K), the initial

work hardening component decreased, and the flow softening appeared to be steady. The initial work hardening occurred at relatively low strain levels when temperatures lower than 623 K were employed. This hardening was followed by mild flow softening, and a dynamic balance between work hardening and softening was eventually reached. In addition, a comparison of the stress–strain curves with those of other AZ series commercial Mg alloys [22] revealed that the peak strain (ε_p) corresponding to the peak stress of the experimental alloy was small.
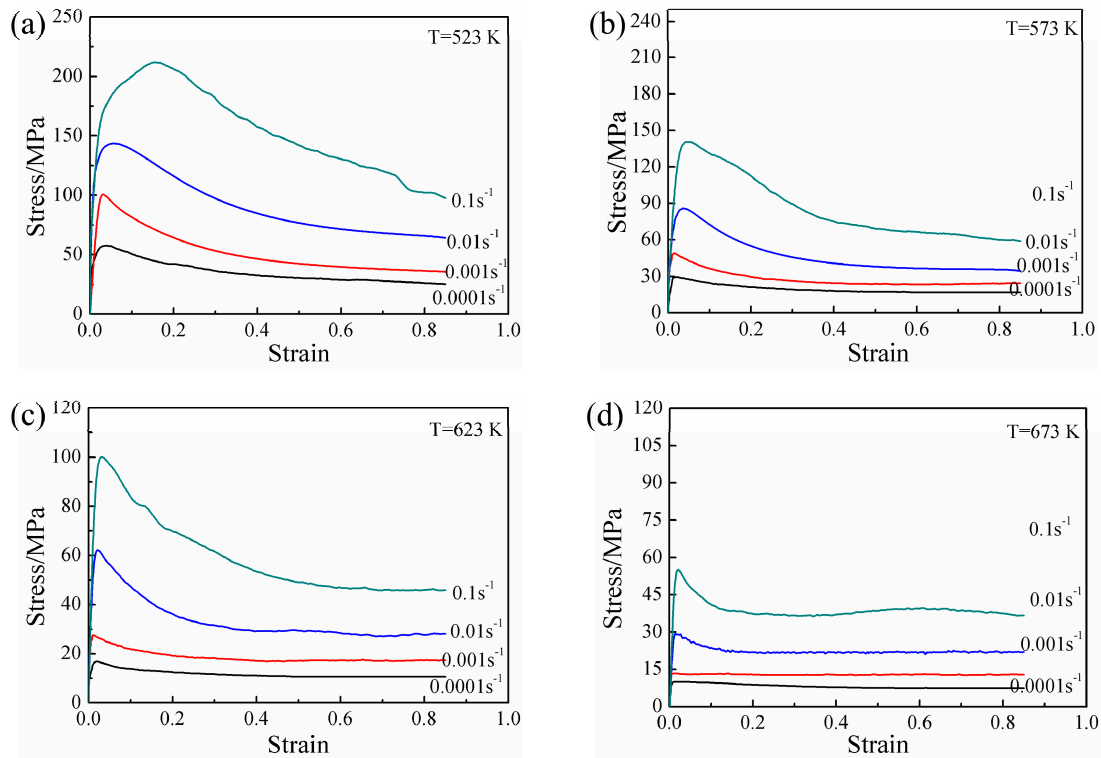

Figure 5. True stress–strain behavior of experimental alloy obtained by hot compression tests at different temperatures: (**a**) 523 K, (**b**) 573 K, (**c**) 623 K, and (**d**) 673 K.

3.4. Constitutive Analysis

Research on different materials reveals that thermal deformation is a process controlled by thermal activation. The deformation behavior was greatly affected by strain rate and deformation temperature. According to the characteristics of the flow stress–strain curves, the relationship between flow stress and deformation conditions (temperature and strain rate) can be expressed by the hyperbolic sine Arrhenius-type equation proposed by Sellars [23]:

$$\dot{\varepsilon} = A[\sinh(\alpha\sigma)]^n \exp\left(-\frac{Q}{RT}\right) \tag{1}$$

where $\dot{\varepsilon}$ is the strain rate, A (s^{-1}) and α (MPa^{-1}) are the material constants, σ is the flow stress (MPa), n is the stress index, R is the general gas constant (8.314 J·mol^{-1}K^{-1}), T is the absolute temperature (K), and Q is the activation energy of thermal deformation (KJ/mol). Equation (1) can be expressed as two power-law expressions, which are expressed as Equations (2) and (3), under low-stress and high-stress conditions, respectively [24]:

$$\dot{\varepsilon} = A_1\sigma^{n_1} \exp\left(-\frac{Q}{RT}\right) \tag{2}$$

$$\dot{\varepsilon} = A_2 \exp(\beta\sigma) \exp\left(-\frac{Q}{RT}\right) \tag{3}$$

where A_1, A_2, $\beta = \alpha n_1$ are material constants. The maximum stress (peak stress σ_p) in the flow curve can be used as the representative stress of each flow curve [25]. To study the flow characteristics of Mg-16Al Mg alloy during hot working after solution treatment, the peak stress, σ_p, was used to calculate the constitutive equation parameters in this work. After taking the natural logarithms for both sides of Equations (1)–(3), it is found that n, n_1, and β are the slopes obtained from the linear fitting results of the curves of $\ln\dot{\varepsilon}$ versus $\ln\sigma$, σ, and $\ln[\sinh(\alpha\sigma)]$, respectively, as shown in Figures 6 and 7a. The n_1, β, n, and α values of the experimental alloys under various deformation conditions were 4.437, 0.084, 2.840, and 0.0189, respectively.
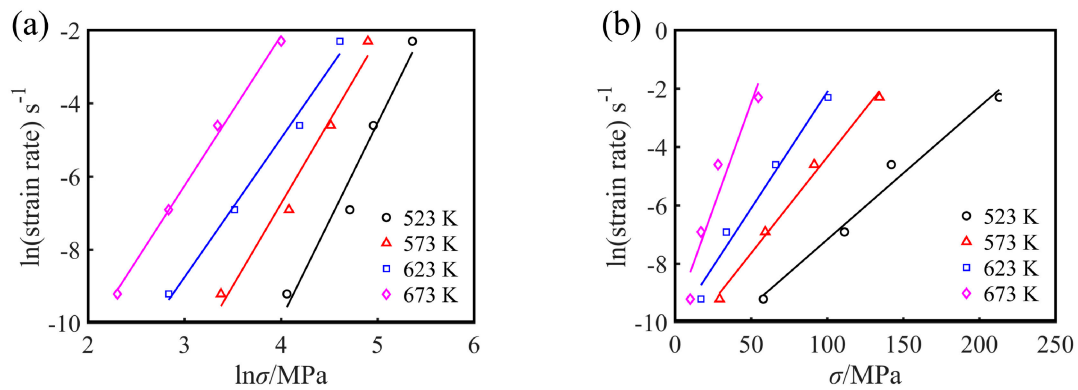

Figure 6. (**a**) $\ln\dot{\varepsilon}$-$\ln\sigma$ and (**b**) $\ln\dot{\varepsilon}$-σ linear regression curves for the experimental alloy.
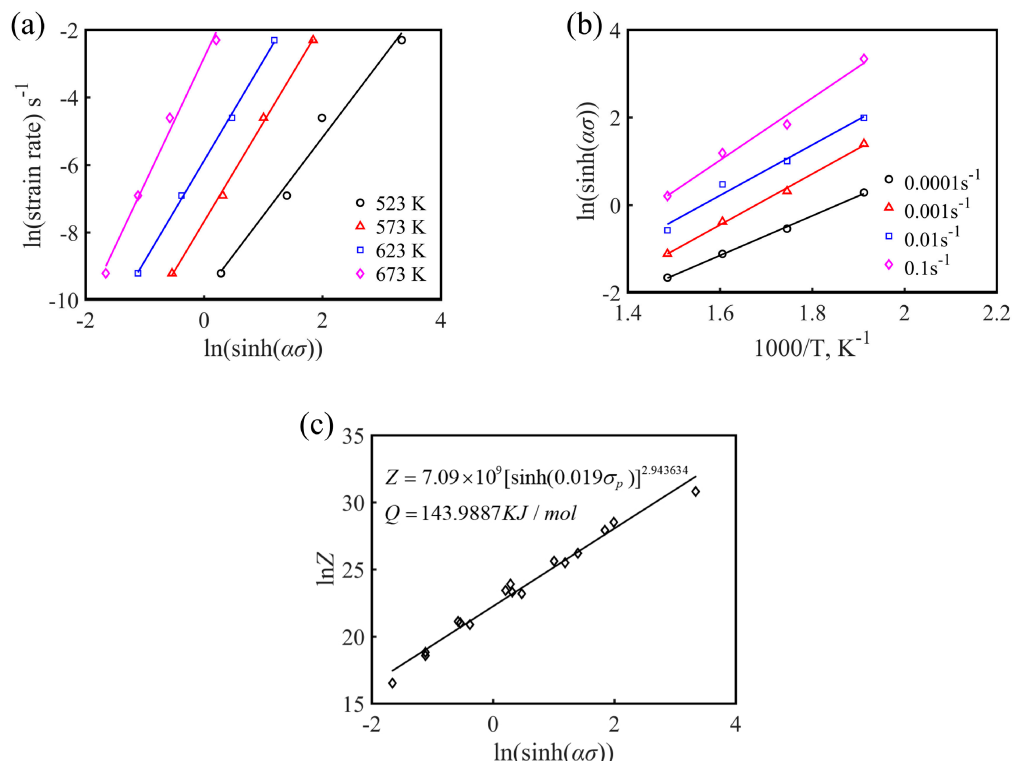

Figure 7. (**a**) $\ln\dot{\varepsilon}$-$\ln[\sinh(\alpha\sigma)]$, (**b**) $\ln[\sinh(\alpha\sigma)]$-1000/T, and (**c**) $\ln Z$-$\ln[\sinh(\alpha\sigma)]$ linear regression relationship for the experimental alloy.

According to Equation (1), the deformation activation energy Q can be defined as

$$Q = R\left[\frac{\partial \ln \dot{\varepsilon}}{\partial \ln[\sinh(\alpha\sigma)]}\right]\Bigg|_T \cdot \left[\frac{\partial \ln[\sinh(\alpha\sigma)]}{\partial(1/T)}\right]_{\dot{\varepsilon}} = RnS \tag{4}$$

where the stress index, *n*, is the average slope of the $\ln\dot{\varepsilon}$-$\ln[\sinh(\alpha\sigma)]$ linear fitting curves at a certain temperature, and S is the average slope of the $\ln[\sinh(\alpha\sigma)]$-1/T linear fitting curves at a certain strain rate. According to the linear fitting results of Figure 7a,b, the average activation energy *Q* of Mg-16Al Mg alloy under different deformation conditions can be calculated to be 143.99 KJ·mol^{-1}.

Additionally, the constitutive equation parameters (*Q*, *α*, and *n*) obtained for different types of AZ-based deformed Mg alloys [22] under various deformation conditions were summarized, as shown in Table 1. The *Q* of the experimental alloy was greater than the values of AZ41, AZ61, and AZ80. Moreover, this value was far greater than the activation energy of grain boundary self-diffusion in Mg (92 kJ/mol) [26], which was higher than that of lattice self-diffusion energy in Mg (135 kJ/mol) [27]. However, the *Q* value was close to the diffusion activation energy of Al in Mg (143 KJ/mol), indicating that the rate control mechanism of the alloy during the initial deformation was solute diffusion [28]. The *Q* values of AZ41, AZ61, and AZ80 decreased with increasing Al content. The reason was that the β-Mg$_{17}$Al$_{12}$ phase particles become softened at temperatures exceeding 423 K [29], and the second phase particles at the GBs weaken the obstacles to dislocation motion, thereby reducing the deformation activation energy of the alloy. However, for the experimental alloy, the relatively high deformation activation energy may be explained in terms of two effects. On the one hand, the solution treatment was performed prior to the plastic deformation, but many of the Al atoms were only partly dissolved in the alloy matrix. To a certain extent, the barrier effect of β-Mg$_{17}$Al$_{12}$ phases at the GBs and the Mg$_{17}$Al$_{12}$ phases precipitated from the matrix during the deformation was weakened. The number of particles in the second phase was more than that of other alloys, and the inhibition effect was negligible. On the other hand, numerous Al atoms dissolved in the matrix increased the hindrance to dislocation motion, thereby increasing the energy required for dislocation cross slip and climb.

Table 1. The *Q*, *α*, and *n* values of various extruded AZ Mg alloys.

	Q (KJ/mol)	*α* (MPa^{-1})	*n*
AZ41	130	0.010	4.1
AZ61	115	0.004	5.3
AZ80	105	0.004	3.3
Mg-16Al	144	0.019	3.0

A different stress index, *n*, reflects different creep mechanisms. When *n* is 2, the grains can rotate with each other, the grain boundaries can be coordinated, and slip can occur; when *n* is 3, the grains of the matrix larger, with fewer and coarse grain boundaries, solute dragging the grain boundaries will occur, at which time the dislocation slip creep becomes the main deformation mechanism; when *n* is 5, the creep mechanism is the dislocation creep controlled by climbing [30]. The *n* value of Mg-16Al Mg alloy was approximately equal to 3 under different strain conditions, which was lower than that of other AZ-based Mg alloys, indicating that the deformation mechanism of the alloy during deformation was controlled by dislocation slip.

The influence of temperature and strain rate on the flow behavior can also be expressed by the Zener–Holloman (*Z*) parameter, which is given by Equation (5):

$$Z = A[\sinh(\alpha\sigma)]^n = \dot{\varepsilon}\exp\left(\frac{Q}{RT}\right) \tag{5}$$

Taking the natural logarithm on both sides of Equation (5), Formula (6) is obtained:

$$\ln Z = \ln A + n\ln[\sinh(\alpha\sigma)] \tag{6}$$

Figure 7c shows the results of the linear regression of ln *Z* and ln [$\sinh(\alpha\sigma)$]. The slope, *n*, and intercept ln, *A*, of the experimental alloy were 2.944 and 21.696, respectively, and the corresponding *A*

value was 7.09×10^9. B substituting the calculated parameter values (n, α, Q, and A) into Equation (1), the hot deformation constitutive equation of the Mg-16Al Mg alloy can be obtained.

As shown in Figure 7c, it can be clearly found that the change of peak stress, σ_p, and Z value exhibited a good linear relationship, and the Z value increased with the increase of the peak stress value, σ_p, which indicated that the constitutive equation established was effective. The equation describing the relationship between the peak stress, σ_p, and the Z parameter is as follows:

$$\sigma_p = \frac{1}{0.0189} \ln \left\{ \left(\frac{Z}{7.09 \times 10^9} \right)^{\frac{1}{2.984}} + \left[\left(\frac{Z}{7.09 \times 10^9} \right)^{\frac{2}{2.984}} + 1 \right]^{\frac{1}{2}} \right\} \tag{7}$$

$$Z = \dot{\varepsilon} \exp(\frac{143.989}{RT}) \tag{8}$$

3.4.1. Compensation of Strain

The influence of strain on the thermal deformation behavior of metallic materials is considered (in general) negligible, and, hence, the influence of strain is neglected in Equation (1). However, many studies have shown that the strain variable has a significant effect on the deformation activation energy and material constants in the entire strain range [31–36]. To further explore the flow deformation behavior of the Mg-16Al Mg alloy, α, n, Q, and ln$A$ values were obtained under different strains based on experimental data. Figure 8 shows the α, n, Q, and ln$A$ values of the experimental alloy as a function of the strain. Each value varied significantly with the strain. Therefore, the effect of strain must be considered in order to obtain a constitutive equation that accurately describes the thermal deformation behavior. To incorporate the influence of strain into the equation, the activation energy, Q, and the material constants (α, n, and ln$A$) are assumed to be polynomial functions of the strain [25].
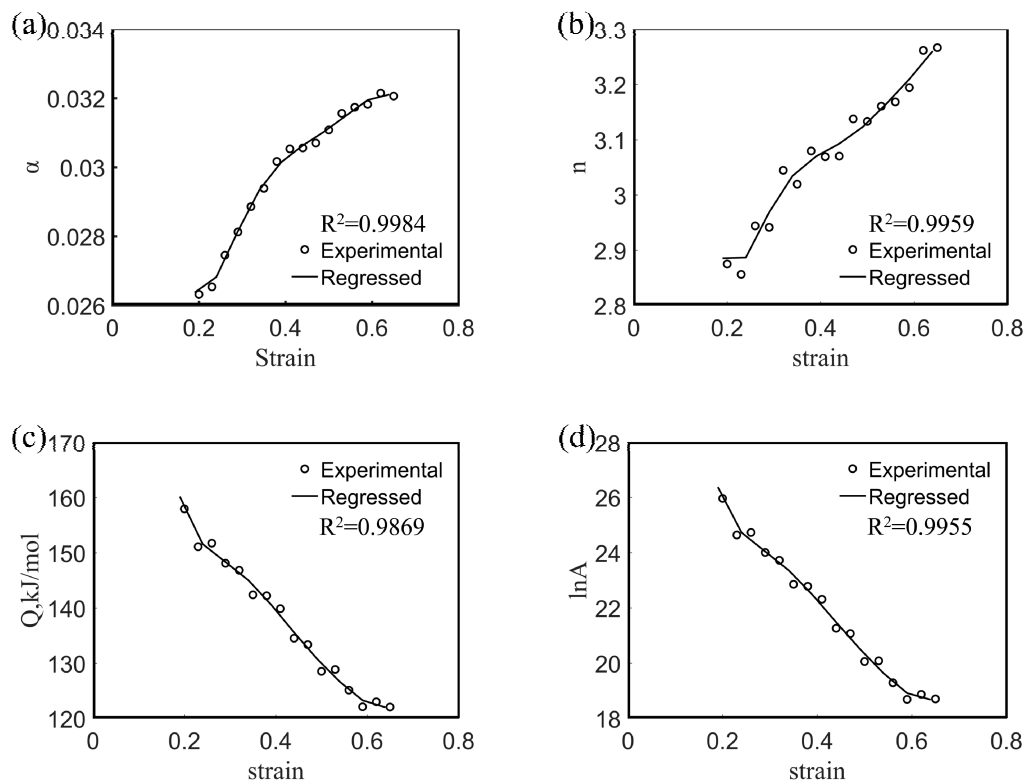

Figure 8. Variations of α (**a**), n (**b**), Q (**c**), and ln$A$ (**d**) with true strain based on sixth-order polynomial-fit for the experimental alloy.

According to the literature [20], the sixth-degree polynomial functions between the material constants and the true strain are given as follows:

$$
\begin{cases}
\alpha = A_0 + A_1\varepsilon + A_2\varepsilon^2 + A_3\varepsilon^3 + A_4\varepsilon^4 + A_5\varepsilon^5 + A_6\varepsilon^6 \\
n = B_0 + B_1\varepsilon + B_2\varepsilon^2 + B_3\varepsilon^3 + B_4\varepsilon^4 + B_5\varepsilon^5 + B_6\varepsilon^6 \\
Q = C_0 + C_1\varepsilon + C_2\varepsilon^2 + C_3\varepsilon^3 + C_4\varepsilon^4 + C_5\varepsilon^5 + C_6\varepsilon^6 \\
\ln A = D_0 + D_1\varepsilon + D_2\varepsilon^2 + D_3\varepsilon^3 + D_4\varepsilon^4 + D_5\varepsilon^5 + D_6\varepsilon^6
\end{cases}
\tag{9}
$$

The polynomial functions (9) were fitted based on the material constants and activation energies obtained under different true strain conditions. The coefficients of the sixth-order polynomial functions are shown in Table 2, and the fitting curves are shown in Figure 8. As shown in the figure, the experimental data exhibited good correlation with the material constant obtained via polynomial function fitting. After the deformation activation energy and material constants are determined from the fitting function, the flow stress under specific strain conditions can be predicted as follows:

$$
\sigma = \frac{1}{\alpha(\varepsilon)}\ln\left\{\left(\frac{Z(\varepsilon)}{A(\varepsilon)}\right)^{1/n(\varepsilon)} + \left[\left(\frac{Z(\varepsilon)}{A(\varepsilon)}\right)^{2/n(\varepsilon)} + 1\right]^{1/2}\right\}, \ Z = \dot{\varepsilon}\exp\left(\frac{Q}{RT}\right)
\tag{10}
$$

Table 2. Polynomial fitting results of α, n, Q, and $\ln A$ for the Mg-16Al alloy.

α	n	Q	$\ln A$
$A_0 = 0.0500$	$B_0 = 2.8496$	$C_0 = 317.7512$	$D_0 = 56.8524$
$A_1 = -0.3767$	$B_1 = -2.0641$	$C_1 = -2266.6117$	$D_1 = -439.7272$
$A_2 = 2.1786$	$B_2 = 5.9022$	$C_2 = 12{,}292.0656$	$D_2 = 2400.9266$
$A_3 = -5.8648$	$B_3 = 31.2201$	$C_3 = -34{,}827.3340$	$D_3 = -6850.4428$
$A_4 = 8.2490$	$B_4 = -133.3649$	$C_4 = 52{,}452.9061$	$D_4 = 10{,}374.5083$
$A_5 = -5.8850$	$B_5 = 173.2873$	$C_5 = -39{,}917.3170$	$D_5 = -7927.3370$
$A_6 = 1.6898$	$B_6 = -75.0813$	$C_6 = 120{,}70.3772$	$D_6 = 2403.0213$

3.4.2. Verification of Constitutive Equation

The predicted values and the measured values of the Mg-16Al experimental alloy under different conditions are compared in Figure 9, and the curves are the true stress–strain curves obtained by the experiment. As the figure shows, the predicted stress values concurred (in general) with the experimental values. However, at low temperature and high strain rate (523 K/0.1 s^{-1}), the predicted values were significantly smaller than the actual values, leading to the failure of the constitutive equation. This may be attributed to two factors, namely (i) numerous twin structures are generated in the experimental alloy during deformation, as shown in Figure 18a, and (ii) the permanent microscopic strength of the Mg$_{17}$Al$_{12}$ phases varied significantly with the temperature, as shown in Figure 10 [37]. Under this deformation condition, many β-Mg$_{17}$Al$_{12}$ phases, which were undissolved in the matrix, became attached to regions near the twin boundaries. However, the γ-Mg$_{17}$Al$_{12}$ phases, which were dissolved in the α-Mg matrix, were re-precipitated from the matrix. At this time, the microscopic strength value of the Mg$_{17}$Al$_{12}$ phase (420 MPa) was considerably greater than the strength of the experimental alloy. These may have resulted in an increase in the overall stress values of the alloy under the condition of low temperature and high strain rate. Consequently, the predicted stress values were lower than the experimental values.
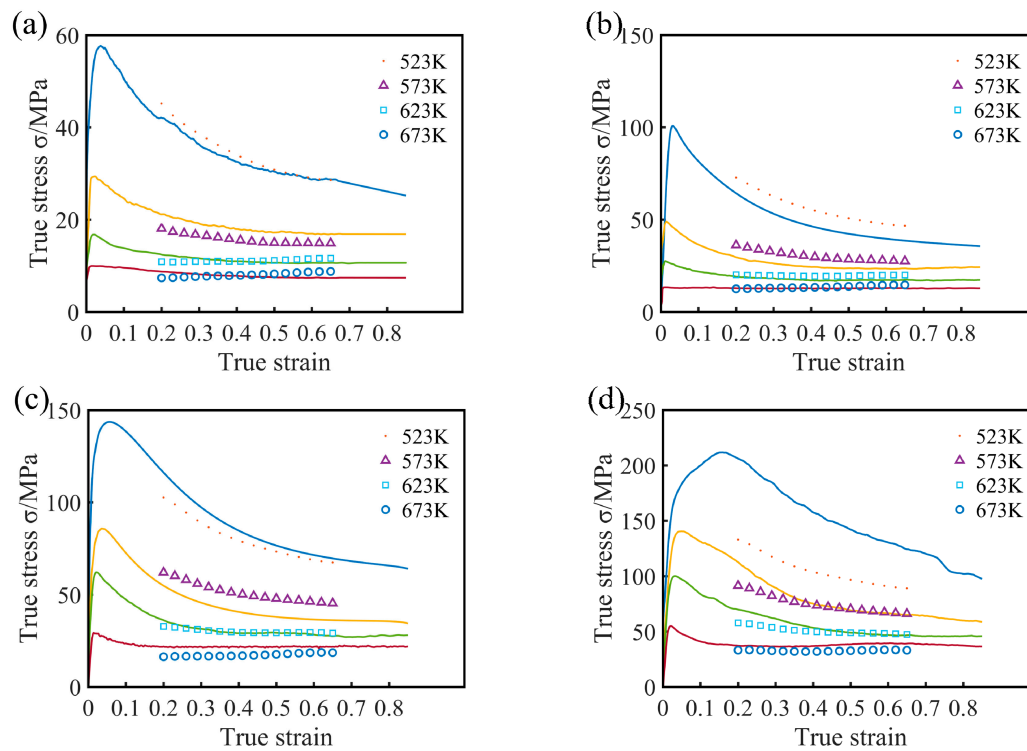
Figure 9. Comparisons between predicted and measured flow stress curves of Mg16Al alloy at different strain rate: (**a**) 0.0001 s^{-1}, (**b**) 0.001 s^{-1}, (**c**) 0.01 s^{-1}, and (**d**) 0.1 s^{-1}.

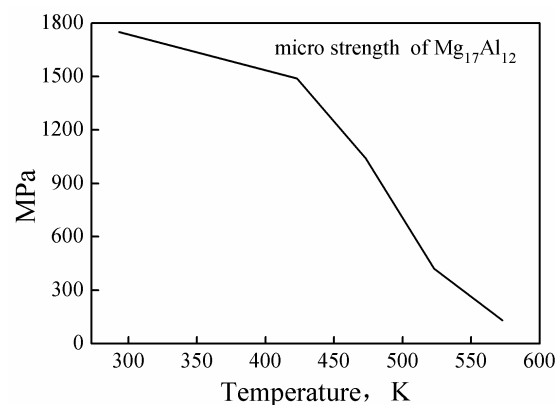**Figure 10.** Permanent microscopic strength values of the $Mg_{17}Al_{12}$ phase at different temperatures. [37].

The accuracy of the constitutive equation was further evaluated, and the predictive power of this equation was quantified. This was achieved by calculating, from Equations (11) and (12) [33], the correlation coefficient (*R*) and the average absolute relative error (AARE, E_R) between the experimental and predicted flow stress values:

$$R = \frac{\sum\limits_{i=1}^{N}(E_i - \overline{E})(P_i - \overline{P})}{\sqrt{\sum\limits_{i=1}^{N}(E_i - \overline{E})^2 \sum\limits_{i=1}^{N}(P_i - \overline{P})^2}} \tag{11}$$

$$E_R = \frac{1}{N}\sum_{i=1}^{N}\left|\frac{E_i - P_i}{E_i}\right| \times 100\% \tag{12}$$

where *E* is the experimental flow stress value, and *P* is the flow stress value predicted by the constitutive equation. Moreover, $\overline{E}$ are $\overline{P}$ the average values of experimental and predicted flow stress, respectively. *N* is the total number of the data in the study.

The correlation coefficient, *R*, represents the linear relationship strength between the experimental and the predicted stress values. The predicted value of the model may be higher or lower (than the actual value), but the *R* value increases non-monotonically with the goodness of the fit [38,39]. Therefore, the unbiased statistical parameter *AARE* was also used in this study, to verify the predictability of the model. *R* and *AARE* values of 0.9565 and 10.6%, respectively, were calculated for large-scale deformation conditions (see Figure 11a). This reflected the good correlation between the experimental data and the predicted data, and a good predictive ability of the proposed constitutive equation was noted. However, a maximum *AARE* value of 33.27% was calculated for deformation conditions such as low temperature and high strain rate (523 K/0.1 s^{-1}). This value indicated that the constitutive model was inapplicable and the equation was invalid. The predicted stress values of the constitutive model were considerably smaller than the experimental stress values, and, therefore, a stress value ($\Delta\sigma$) was added to Equation (10), for improved stress prediction. A comparison of the predicted stress value with the experimental stress value revealed a value of 50 MPa (see Equation (13)) for the constitutive equation corresponding to this condition). Figure 11b shows the comparison between the experimental flow stress values and the predicted stress values after inclusion of the additional stress. Under all deformation conditions, the calculated *R* and *AARE* values were 0.9749 and 9.04%, respectively. After the stress value was added, the flow stress at a temperature of 523 K and a strain rate of 0.1 s^{-1} was accurately predicted by the constitutive equation (i.e., Equation (13)).

$$\sigma = \frac{1}{\alpha}\ln\left\{\left(\frac{Z}{A}\right)^{1/n} + \left[\left(\frac{Z}{A}\right)^{2/n} + 1\right]^{1/2}\right\} + 50, \; Z = 0.1\exp\left(\frac{Q}{4848.222}\right) \tag{13}$$
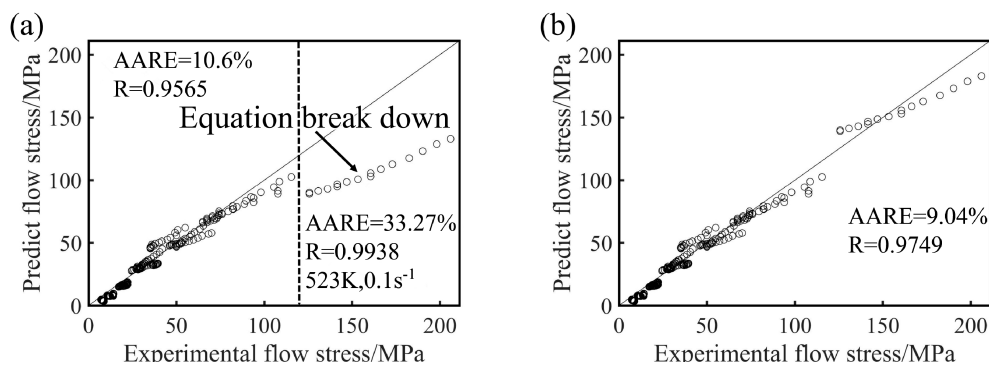

Figure 11. The comparison between the experimental flow stress and the flow stress predicted by the constitutive equation before (**a**) and after (**b**) inclusion of the additional stress.

3.5. Critical Conditions of DRX

Figure 12 shows the typical strain hardening rate ($\theta = d\sigma/d\varepsilon$) versus flow stress ($\sigma$) obtained at 673 K and 0.1 s^{-1}. The θ-σ diagrams can be divided into three distinct stages. The first stage lasted from the initial stress to the critical stress (σ_c), where the value of θ decreased sharply. The second stage encompassed the deformation from DRX (corresponding to σ_c) to the peak stress (σ_p). At this time, DRX began inside the material, and the strain hardening rate decreased with increasing flow stress, until the peak flow stress (corresponding to σ_p) was reached. At σ_p, the work hardening effect and dynamic recrystallization softening effect were balanced. The third segment lasted from σ_p to the steady-state flow stress (corresponding to σ_s), where recrystallization softening played a dominant role. At this time, the flow stress began to decrease, and the strain hardening rate decreased to a negative

value. Upon rebalancing of the recrystallization softening and work hardening processes, the material entered a steady-state flow stage [40].
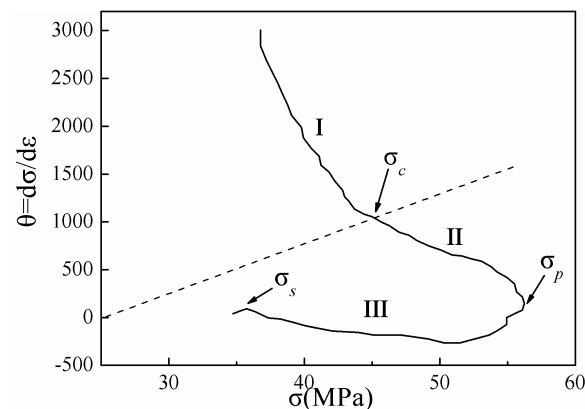

Figure 12. Typical θ–σ plot obtained at 673 K and 0.1 s^{-1}.

Poliak and Jonas [10] proposed a method of determining the critical condition required for DRX by considering the inflection point of strain hardening rate θ–σ (θ = dσ/dε) relation curves. For accuracy of the calculation, the second derivative method was used to obtain the minimum values of ($-$dθ/dσ)–σ relation curves as the critical stress values of DRX, and the corresponding critical strain values were calculated. Figure 13 shows the relation curves between the θ and σ of Mg-16Al Mg alloy under certain deformation conditions. In this study, the critical strain and critical stress values under different deformation conditions were determined via the second derivative method.
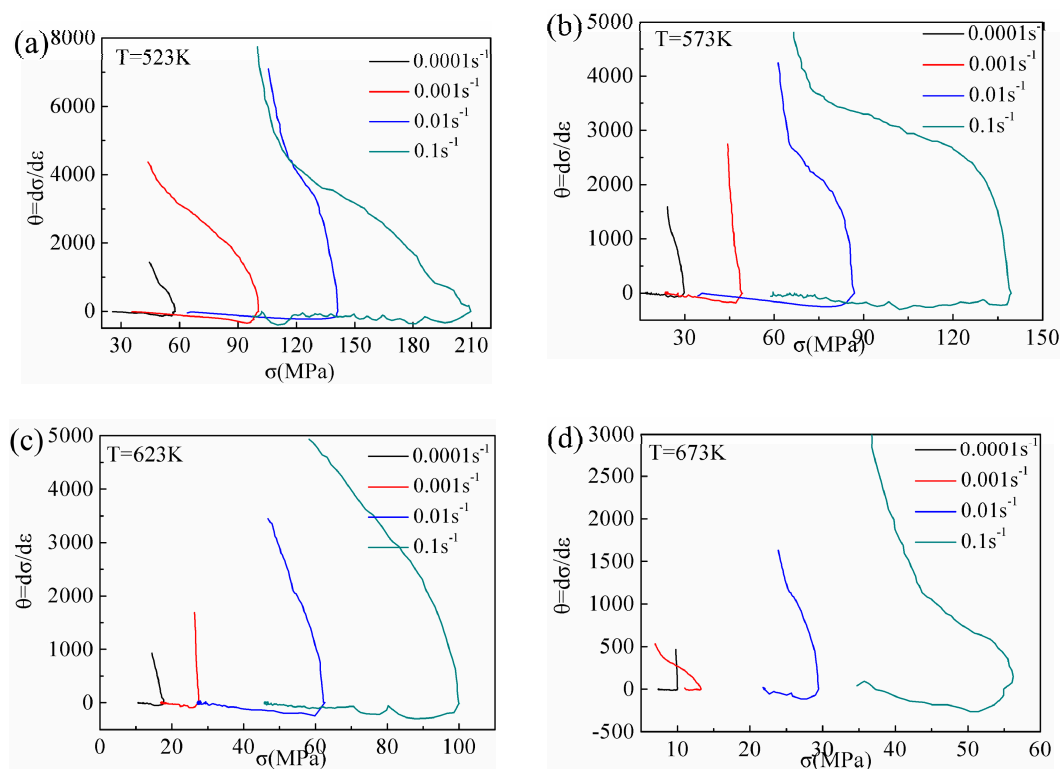

Figure 13. θ-σ curves at different deformation conditions: (**a**) T = 523 K, (**b**) T = 573 K, (**c**) T = 623 K, and (**d**) T = 673 K.

The σ_c and ε_c of DRX are affected by both the temperature and the strain rate (as shown in Figure 14). For a given strain rate, the critical condition values decreased with increasing temperature.

The diffusion rate of atoms increased with increasing deformation temperature, and the dislocations were prone to slip and climb. Moreover, the propensity for grain boundary slip increased, which was conducive to the occurrence of DRX. For a given temperature, the critical condition values increased with increasing strain rate. The time for dislocation movement was insufficient under high strain rate conditions, and, hence, elimination of the internal stress in the grains was difficult, resulting in aggregation of the dislocations. Similarly, the nucleation and growth time of recrystallized grains was also insufficient, which was unfavorable for the occurrence of DRX.
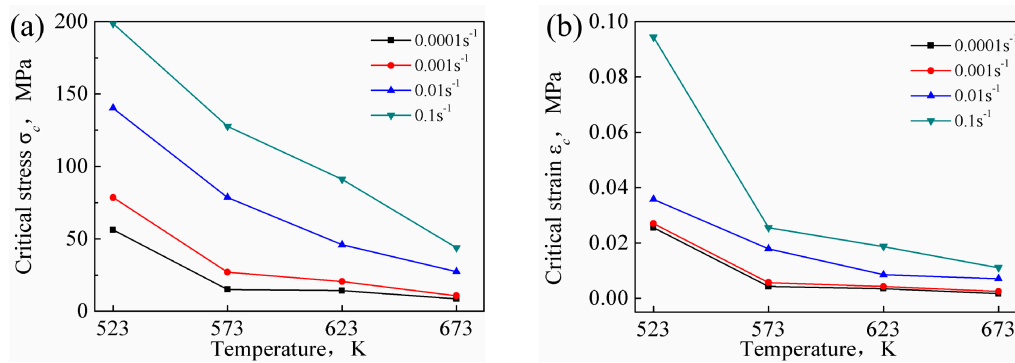

Figure 14. σ_c-T curves (**a**) and ε_c-T curves (**b**) at different deformation conditions.

The critical stress values for DRX of the Mg-16Al Mg alloy were lower than that of other AZ-based Mg alloys [16,17], indicating that several $Mg_{17}Al_{12}$ phases hindered grain boundary migration. The consequent grain growth inhibition yielded uniform and fine grains. Moreover, many $Mg_{17}Al_{12}$ phase particles obstructed dislocation movement, causing dislocation accumulation, and the accumulation sites served as DRX nucleation points. This promoted the nucleation of recrystallized grains, and these regions were prone to DRX.

To further illustrate the effect of strain rate and temperature on the ε_c of DRX, the Sellars model [14] was introduced to characterize the ε_c model:

$$\varepsilon_c = aZ^b \tag{14}$$

where *a* and *b* are constants and *Z* is the Zener–Hollomon parameter. The average activation energy *Q* of Mg-16Al Mg alloy under different deformation conditions was 143.99 KJ/mol. The logarithm of both sides of Equation (14) is taken as follows:

$$\ln \dot{\varepsilon} = \ln a + b \ln Z \tag{15}$$

The ε_c, *Q*, and microstructure of the experimental alloy were analyzed. For different strain rates, the single-factor linear regression of $\ln\varepsilon_c$-$\ln Z$ was performed (see Figure 15a), and Equation (16) described the critical strain prediction model of the Mg-16Al Mg alloy. The results of the model revealed that the high deformation temperature reduced the *Z* parameter and the critical strain, ε_c, of DRX, thereby promoting the occurrence of DRX. However, the high strain rate led to an increase in the Z-parameter, and, hence, the ε_c required the occurrence of DRX, thereby suppressing the occurrence of DRX.

Univariate linear regression was performed on the ε_c versus peak strain (ε_p) curves of the Mg-16Al Mg alloy (see Figure 15b for the linear relationship). The linear regression results of the ε_c-ε_p curves can be described by Equation (17), which showed that DRX occurred before the peak strain was reached.

$$\varepsilon_c = 1.32 \times 10^{-4} Z^{0.18643} \tag{16}$$
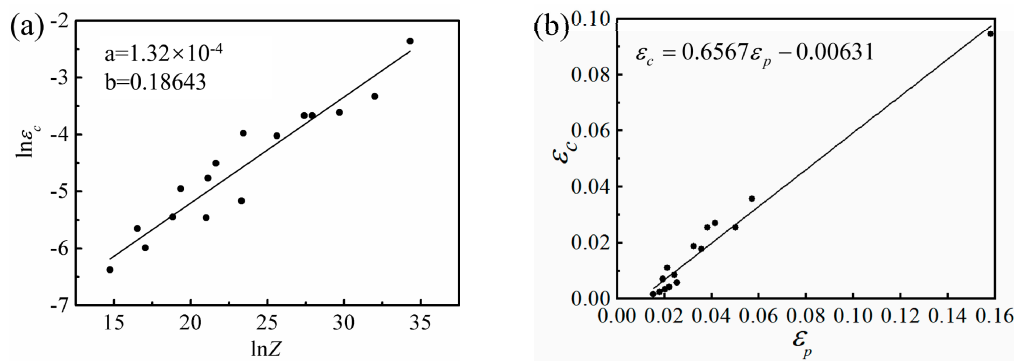
$$\varepsilon_c = 0.6567 \varepsilon_p - 0.00631 \tag{17}$$

Figure 15. $\ln\varepsilon_c$-$\ln Z$ relationship curve (**a**) and ε_p–ε_c relationship curve (**b**).

3.6. Hot Processing Map

Processing maps based on dynamic material model theory are considered to be effective methods for optimizing the hot working parameters of many metals and alloys over a wide range of temperatures and strain rates. In this model, the workpiece is regarded as an energy dissipator, and the instantaneous power during plastic deformation is given as follows [41]:

$$P = \int_0^{\dot{\varepsilon}} \sigma d\dot{\varepsilon} + \int_0^{\sigma} \dot{\varepsilon} d\sigma = G + J \tag{18}$$

where σ is the flow stress, and $\dot{\varepsilon}$ is the strain rate. The first integral is expressed in G, which represents the energy consumed by plastic deformation of materials, most of which is converted into heat energy, and a small part is stored in the form of crystal defect energy. The second integral is expressed in J, which represents the energy consumed by the evolution of microstructure during the plastic deformation of materials. The distribution ratios of G and J can be described by the strain rate sensitivity index, m, of flow stress:

$$m = \frac{dJ}{dG} = \frac{\dot{\varepsilon}d\sigma}{\sigma d\dot{\varepsilon}} = \frac{d\log\sigma}{d\log\dot{\varepsilon}} \tag{19}$$

According to m, the dimensionless power dissipation efficiency, η, relative to microstructural changes, can be obtained as follows:

$$\eta = \frac{J}{J_{\max}} = \frac{2m}{m+1} \tag{20}$$

The power dissipation diagram is the contour map of the power dissipation efficiency, η, drawn on the $\ln\dot{\varepsilon}$-T two-dimensional plane under a certain strain. The metallographic observation can be used to analyze the deformation mechanism of different regions with the power dissipation efficiency map. Based on the extreme principles of irreversible thermodynamics, the continuous instability criterion is defined as follows [42]:

$$\xi(\dot{\varepsilon}) = \frac{\partial\ln[m/(m+1)]}{\partial\ln\dot{\varepsilon}} + m \le 0 \tag{21}$$

The instability map consisting of $\xi(\dot{\varepsilon})$, $\ln\dot{\varepsilon}$, and T, and when the unstable parameter $\xi(\dot{\varepsilon})$ is negative, indicating that the rheological instability such as wedge cracking, localized deformation, shear deformation, and so on has occurred.

According to Equations (20) and (21), η and $\xi(\dot{\varepsilon})$ values under different strain conditions can be obtained, and the hot processing maps can be obtained by superposing the power dissipation diagrams and instability diagrams. The hot processing maps under different strains are shown in Figure 16.
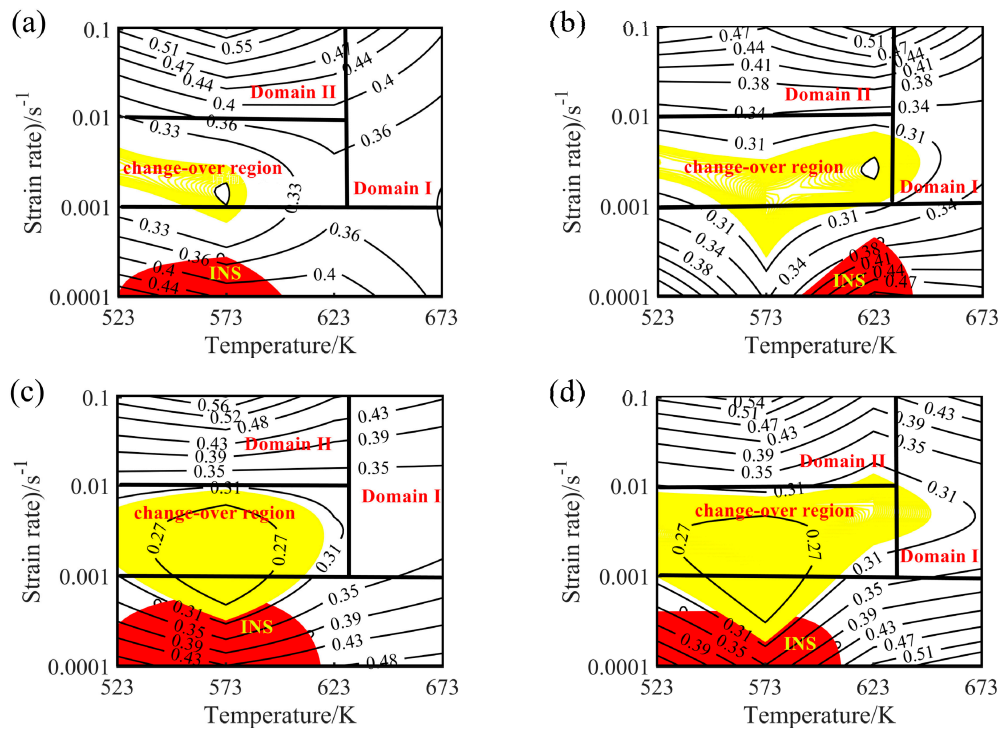
Figure 16. Processing maps for the experimental alloy at different true strains: (**a**) 0.2, (**b**) 0.3, (**c**) 0.4, and (**d**) 0.6. Four different areas can be distinguished, namely a workability region (Domain I), a metastable workability region (Domain II), a transition region (change-over region), and an unsuitable workability region, i.e., instability region (INS).

The contour lines in the hot processing map represent the value of energy dissipation efficiency, the yellow area represents the transition region (change-over region), and the red area represents the instability area (INS). The value of power dissipation efficiency greater than 30% is suitable for hot deformation of Mg alloys [43]. Generally speaking, the dissipation efficiency increases with the increase of temperature and the decrease of strain rate. Similarly, the dissipation efficiency of Mg-16Al Mg alloy increases with increasing temperature. However, when the strain rate ranges from 0.001 to 0.1 s^{-1}, the values of power dissipation efficiency increase with the increase of the strain rates. While the strain rate ranges from 0.0001 to 0.001 s^{-1}, the values of power dissipation efficiency decrease with the increase of the strain rates.

The hot processing maps of the Mg-16Al Mg alloy under different strain conditions are shown in Figure 16. Four different areas can be clearly distinguished, namely a workability region (Domain I), a metastable workability region (Domain II), a transition region (change-over region), and an instability region (INS). The area of the change-over region and the INS increased significantly with an increasing amount of strain. Figure 17 shows the microstructure of the alloy under different deformation conditions in the workability region. These results confirmed that microstructural evolution was correlated with the value of the power dissipation efficiency. In Domain I (633–673 K and 0.001–0.1 s^{-1}), the peak value of the efficiency was ~45%. The high deformation temperature enhanced thermal activation and promoted grain boundary sliding. Furthermore, the initiation of non-basal slip systems and the increasing dislocation density during the thermal deformation process facilitated the nucleation of DRX. In addition, the movement of dislocations was hindered by many β-Mg$_{17}$Al$_{12}$ phases distributed in a discontinuous network at the GBs and the Mg$_{17}$Al$_{12}$ phases precipitated from the α-Mg matrix. This resulted in the accumulation of dislocations, and the accumulation sites became the nucleation sites for DRX. Figure 17 shows the microstructure after deformation at 673 K and different strain rates. The microstructure consisted of a uniform equiaxed structure, with a small amount of elongated β-Mg$_{17}$Al$_{12}$ phase sandwiched at the GBs. With decreasing strain rate, the DRX grains had sufficient

time to grow, and the average grain size increased from 12 μm at a strain rate of 0.1 s^{-1} to 22 μm at a strain rate of 0.001 s^{-1}. Due to the large number of Al atoms in the experimental alloy, $Mg_{17}Al_{12}$ phases were inevitably precipitated at the GBs and inside the grains. Decreasing strain rate led, however, to a reduction in the precipitation of these phases from the matrix within the GBs and grains (except for the discontinuous bulk β-$Mg_{17}Al_{12}$ phases). At a strain rate of 0.001 s^{-1}, only a small amount of $Mg_{17}Al_{12}$ phases precipitated at the GBs.

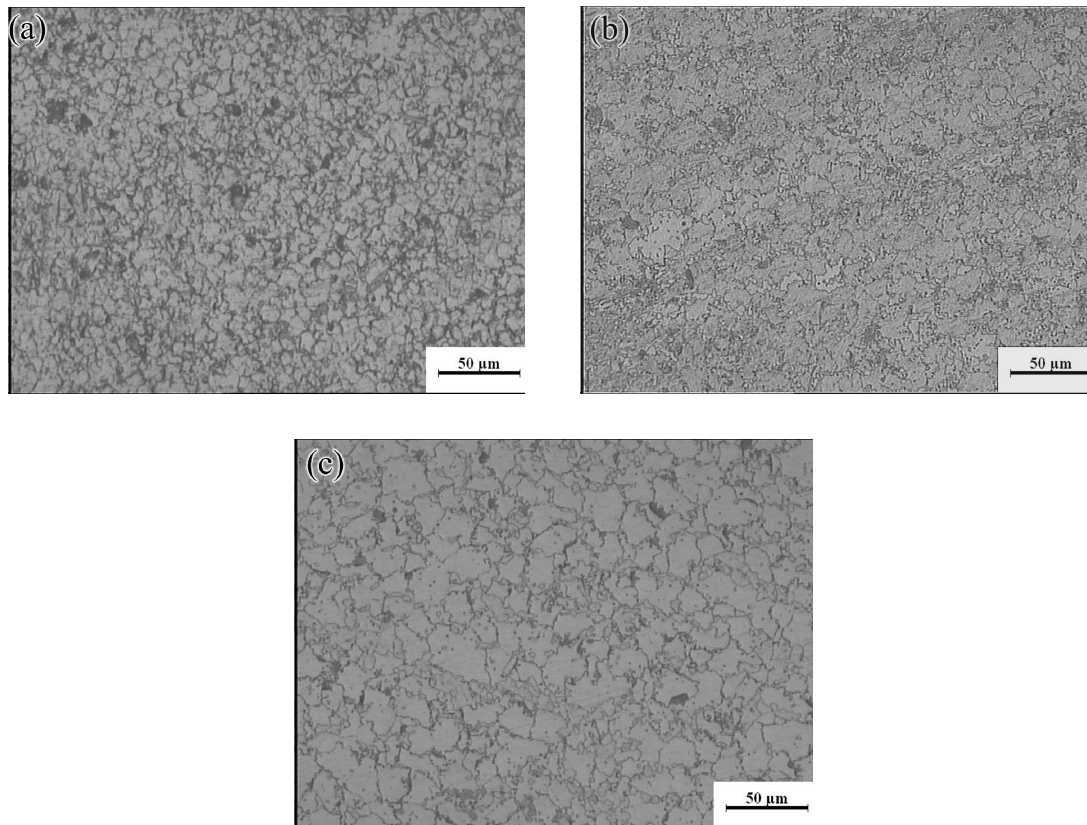**Figure 17.** Microstructures of the Mg-16Al Mg alloy in Domain I: (**a**) 673 K/0 0.1 s^{-1}, (**b**) 673 K/0 0.01 s^{-1}, and (**c**) 673 K/0 0.001 s^{-1}.

Domain II was characterized by a peak dissipation efficiency value of 60% (523–623 K and 0.01–0.1 s^{-1}). Unfortunately, although the dissipation value in this region was high and increased with increasing strain rate, the deformed specimen will generate high local viscosity heat, due to the high strain rate. This may lead to the generation of local shear bands and microcracks. Figure 18a shows the plastic deformation at a temperature of 523 K and a strain rate of 0.1 s^{-1}. Considerable dislocation proliferation and entanglement occurred during the deformation process. The corresponding formation of numerous β-$Mg_{17}Al_{12}$ phases increased the hindrance to dislocation motion, resulting in a large stress concentration at the GBs and, consequently, crack initiation. In addition, at low temperatures (<573 K), basal slip was the dominant deformation mechanism, with only a small amount of cylindrical slip and conical slip occurring along favorable orientations. During deformation, twin nucleation was promoted, and the number of sub-crystals increased. The coordinated plastic deformation of these crystals in subsequent deformation may lead to a chain-like recrystallization structure (see Figure 18a), and partially DRX grains appeared near the β-$Mg_{17}Al_{12}$ phases and the GBs. With increasing temperature, dislocation climb and slip became easier than at lower temperatures. The increase in dislocation density during deformation facilitated the nucleation of DRX. Many fine DRX grains appeared in the microstructure, as shown in Figure 18b. When the deformation temperature reached 623 K, the σ_c of non-basal surface slip decreased, the degree of stress concentration was significantly reduced, and the

atomic thermal activation capacity was enhanced. At this time, each sliding system, especially the non-basal surface sliding system, became the dominant means of releasing stress concentration and coordinating plastic deformation. The Mg-16Al Mg alloy underwent continuous DRX at a temperature of 623 K and a strain rate of 0.1 s^{-1}, as shown in Figure 18c. The resulting microstructure consisted of fine equiaxed crystals and several discontinuous $Mg_{17}Al_{12}$ phases that were distributed at the GBs.

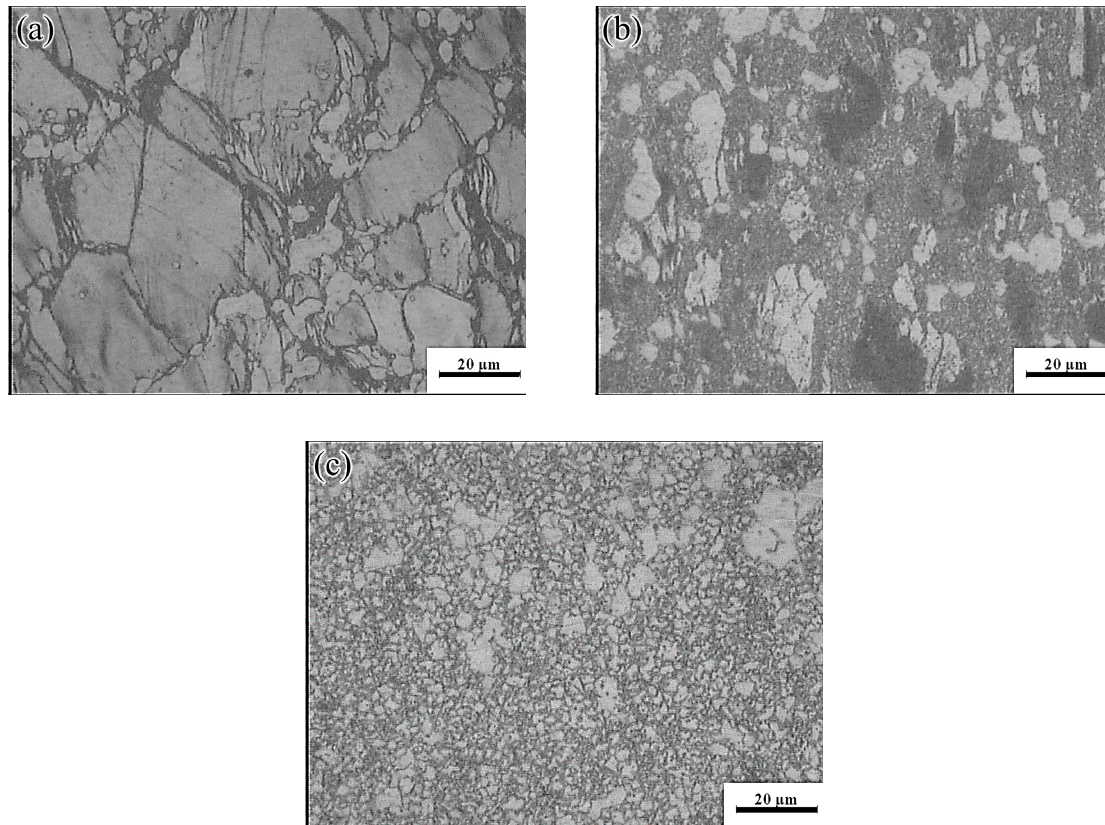**Figure 18.** Microstructures of the Mg-16Al Mg alloy in Domain II: (**a**) 523 K/0 0.1 s^{-1}, (**b**) 573 K/0 0.1 s^{-1}, and (**c**) 623 K/0 0.1 s^{-1}.

The yellow part in the processing map corresponded to the change-over region (523–637 K and 0.001–0.01 s^{-1}; peak power dissipation efficiency: ~30%). The optical micrographs and the SEM images are shown in Figures 19 and 20, respectively. Microstructures undergoing DRX were observed at 573 K and strain rates of 0.01 and 0.001 s^{-1}, respectively. A small amount of massive discontinuous β-$Mg_{17}Al_{12}$ phases was present in these microstructures. Moreover, many discontinuous fine $Mg_{17}Al_{12}$ phases were reprecipitated in the recrystallized grain boundaries and even within the grains. With decreasing strain rate, the average recrystallization grain size increased from 2 to 4 μm. Deformation conditions of 623 K and 0.001 s^{-1} yielded a fully recrystallized coarse-grained microstructure consisting mainly of equiaxed crystals (Figure 19c). The recrystallized grain size increased from 2 μm at 0.1 s^{-1} to 12 μm, and the discontinuous massive β-$Mg_{17}Al_{12}$ phases were distributed on triangular grain boundaries. As shown in Figure 20c, a small amount of dot-like $Mg_{17}Al_{12}$ phases precipitated inside the recrystallized grains.

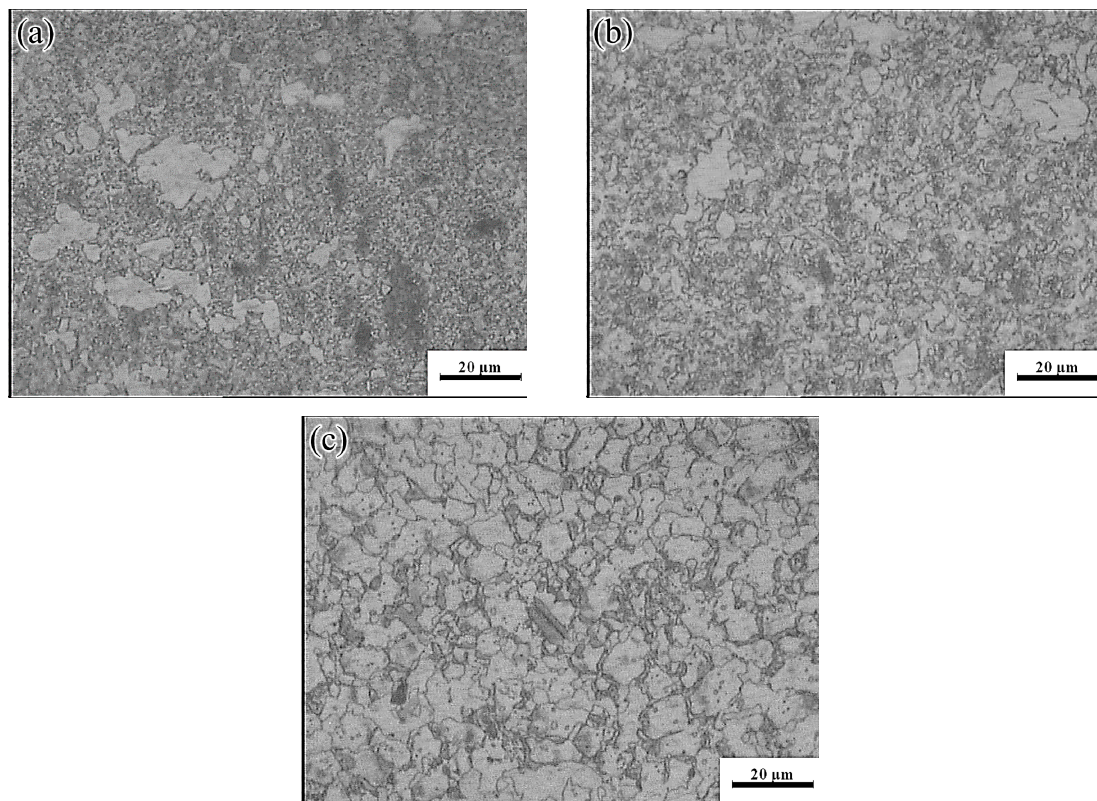**Figure 19.** Microstructures of the Mg-16Al Mg alloy in change-over region: (**a**) 573 K/0 0.01 s^{-1}, (**b**) 573 K/0 0.001 s^{-1}, and (**c**) 623 K/0 0.001 s^{-1}.
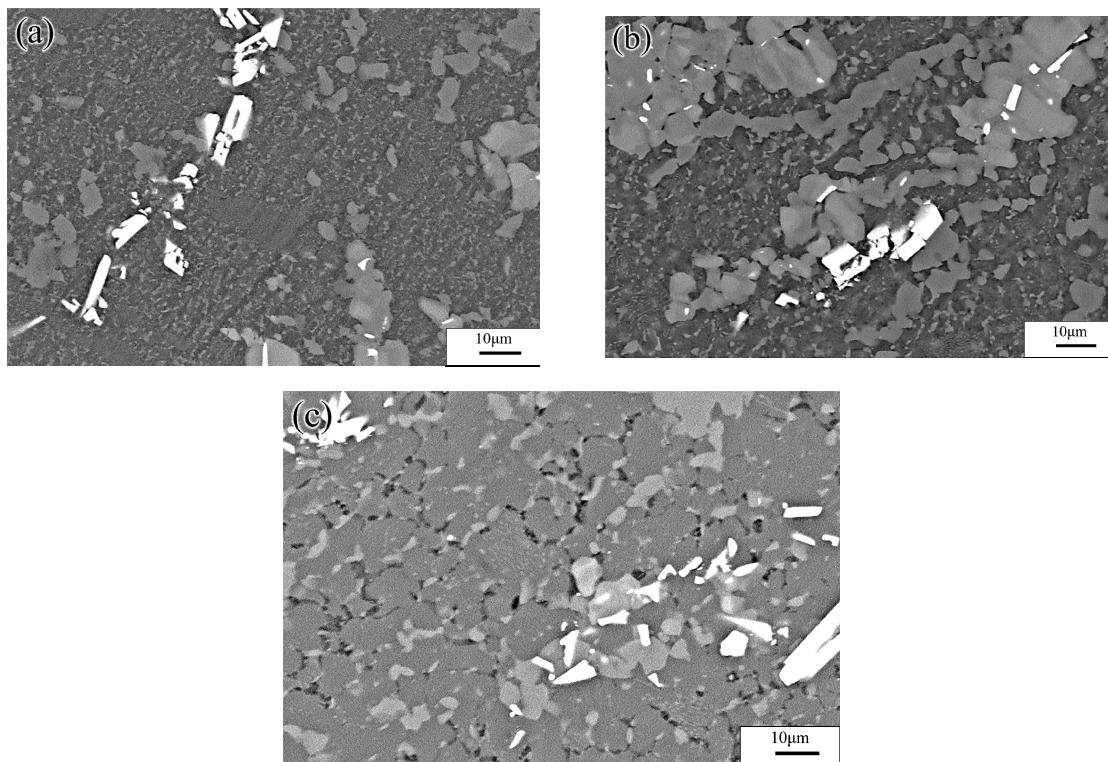
Figure 20. SEM images of the Mg-16Al Mg alloy in change-over region: (**a**) 573 K/0 0.01 s^{-1}, (**b**) 573 K/0 0.001 s^{-1} and (**c**) 623 K/0 0.001 s^{-1}.

A distinct instability region (523–633K and 0.0001–0.001 s^{-1}) was observed in the processing map. As shown in Figure 21, when hot deformation occurred at a low strain rate, each deformed specimen underwent complete DRX (irrespective of the temperature), and the size of the recrystallized grains increased with increasing temperature. The dissipation efficiency was high (peak value: 50%) in the INS, owing to the occurrence of complete DRX. Due to the low strain rate, sufficient time for Al-atoms diffusion, and the high Al content of the alloy specimens, several γ-Mg$_{17}$Al$_{12}$ phases dissolved in the experimental alloy were re-precipitated from the α-Mg matrix.

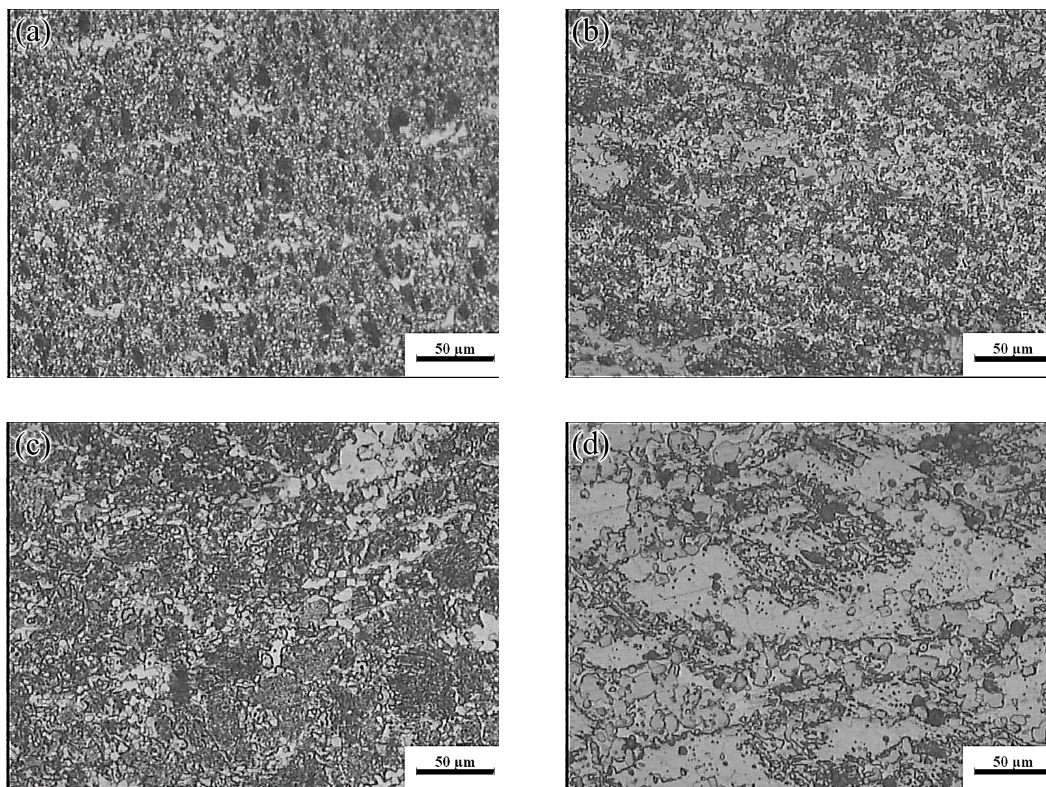**Figure 21.** Microstructures of Mg-16Al Mg alloy in INS: (**a**) 523 K/0.0001 s^{-1}, (**b**) 573 K/0.0001 s^{-1}, (**c**) 623 K/0.0001 s^{-1}, and (**d**) 673 K/0.0001 s^{-1}.

Figure 22a shows SEM images of the specimens deformed at 523 K and 0.0001 s^{-1}. As the results showed, the Mg$_{17}$Al$_{12}$ phases precipitated from the recrystallized grains, and the discontinuous β-Mg$_{17}$Al$_{12}$ phases, which were undissolved in the matrix, occurred throughout the entire specimen microstructure. This may have resulted in the high dissipation efficiency. For deformation at temperatures above 573 K, the sizes of the recrystallized grains increased with increasing temperature. Furthermore, numerous γ-Mg$_{17}$Al$_{12}$ phases precipitated from the recrystallized grains, as shown in Figure 21b,c. Figure 21d shows that, for deformation conditions of 673 K and 0.0001 s^{-1}, the recrystallized grains grew significantly and were elongated along the direction perpendicular to the compression direction. Moreover, except for the bulk β-Mg$_{17}$Al$_{12}$ phases that were undissolved in the matrix, the γ-Mg$_{17}$Al$_{12}$ phases were discontinuously precipitated inside the grains. The INS was observed by means of SEM, as shown in Figure 22. Many microcracks occurred in this region. The generation of numerous Mg$_{17}$Al$_{12}$ phases, microcracks, and vacancies may lead to an increase in the dissipation efficiency. Therefore, hot working in this unstable region should be avoided.
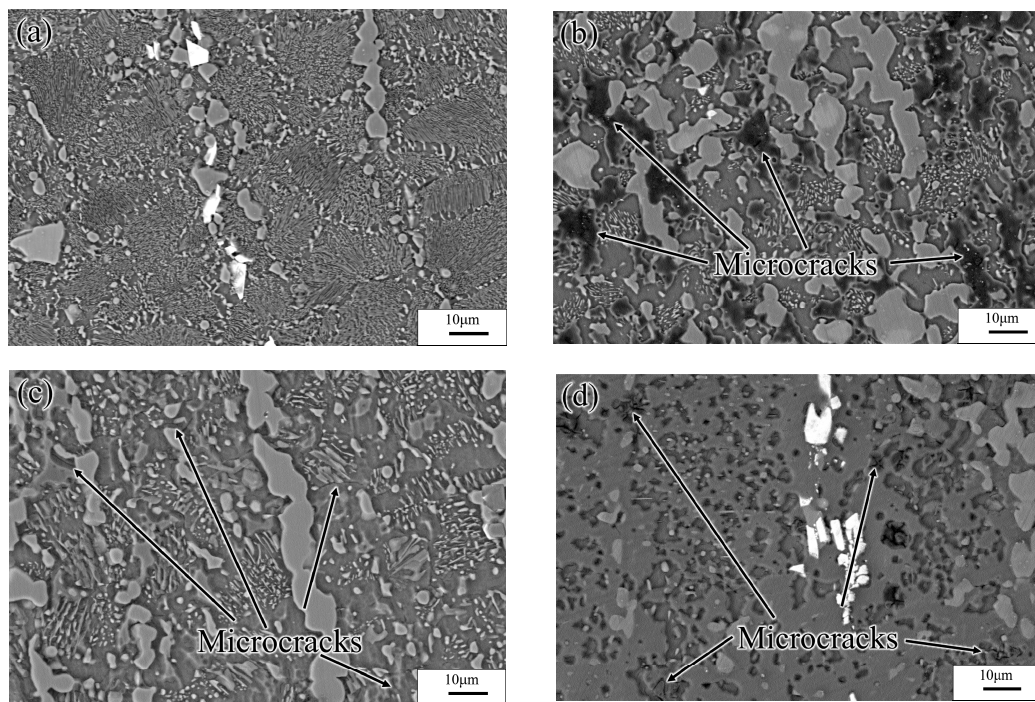
Figure 22. SEM images of Mg-16Al Mg alloy in INS: (**a**) 523 K/0.0001 s^{-1}, (**b**) 573 K/0.0001 s^{-1}, (**c**) 623 K/0.0001 s^{-1}, and (**d**) 673 K/0.0001 s^{-1}.

The hot processing maps and microstructure of the Mg-16Al Mg alloy were analyzed, and this analysis revealed that a high Al content was unfavorable for the plastic forming during hot working. Moreover, compared with other areas, Domain I, which consisted of uniformly sized DRX grains, was associated with high dissipation efficiency and was more suitable for hot working. The window for hot deformation applying the range of test parameters considered was very narrow, as indicated by temperature and strain rate ranges of 633–673 K and 0.001–0.1 s^{-1}, respectively.

4. Conclusions

In the present study, the hot compression deformation behaviors and processing maps of an extruded Mg-16Al Mg alloy bar after solution treatment were investigated under various strain rate (0.0001–0.1 s^{-1}) and temperature (523–673 K) conditions. The major findings are summarized as follows:

- The original extruded microstructure of the Mg-16Al alloy was mainly composed of α-Mg grains, β-Mg$_{17}$Al$_{12}$ phases with discontinuous reticular distribution at the GBs, and γ-Mg$_{17}$Al$_{12}$ phases with a cellular structure inside the α-Mg grain boundaries. After the solution treatment, the discontinuous β-Mg$_{17}$Al$_{12}$ phases were partially dissolved, whereas the γ-Mg$_{17}$Al$_{12}$ phases were completely dissolved in the α-Mg matrix. Massive β-Mg$_{17}$Al$_{12}$ phases persisted at the GBs.
- The Mg-16Al solid solution alloy underwent significant work hardening and continuous flow softening at relatively high strain rate levels ($\dot{\varepsilon} \geq 0.01$ s^{-1}). However, at strain rates lower than these levels, the initial work hardening components of the alloy decreased at high temperatures (T $\geq$ 623 K) and the flow softening appeared as steady-state flow. Nevertheless, at temperatures lower than 623 K, the initial work hardening occurred only at relatively low strains.
- The precipitation of numerous Al-containing second phase particles during the deformation process of the alloy hindered the movement of dislocations and promoted the nucleation of DRX. Consequently, the critical strain, ε_c, of DRX was less than that of the common commercial-grade Mg alloys comprising the AZ series.
- The relatively large number of Al atoms in the Mg-16Al solid solution alloy promoted the nucleation of DRX and refinement of the grains. Similarly, the coordinated interaction between the diffusion

and migration of these atoms and the dislocation movement during hot working deformation reduced the steady-state deformation range. For deformation at high temperatures and low strain rates, the slow dissolution of $Mg_{17}Al_{12}$ phases stimulated the initiation of local microcracks.

- The suitable hot working range of the Mg-16Al Mg alloy after solution treatment was narrow: T = 633–673 K, $\dot{\varepsilon}$ = 0.001–0.1 s^{-1}.

Author Contributions: Conceptualization, Z.W. (Zhongjun Wang) and W.L.; methodology, K.F.; software, Z.W. (Zhenxiong Wei); validation, Z.W., F.H. and J.W.; formal analysis, Z.W. (Zhongjun Wang); resources, Z.W. (Zhongjun Wang); data curation, Z.M.; writing—original draft preparation, Z.M.; writing—review and editing, Z.W. (Zhongjun Wang); funding acquisition, J.W. All authors have read and agreed to the published version of the manuscript.

References

1. Pekguleryuz, M.O.; Kaya, A.A. Creep Resistant Magnesium Alloys for Powertrain Applications. *Adv. Eng. Mater.* **2003**, *5*, 866–878. [CrossRef]

2. Smola, B.; Stulıkova, I.; Buch, F.V.; Mordike, B.L. Structural aspects of high performance Mg alloys design. *Mater. Sci. Eng. A* **2002**, *324*, 113–117. [CrossRef]

3. Liu, H.; Cao, F.; Song, G.L.; Zheng, D.; Shi, Z.; Dargusch, M.; Atrens, A. Review of the atmospheric corrosion of magnesium alloys. *J. Mater. Sci. Technol.* **2019**, *35*, 2003–2016. [CrossRef]

4. Srinivasan, N.; Prasad, Y.V.R.K.; Rama Rao, P. Hot deformation behaviour of Mg–3Al alloy—A study using processing map. *Mater. Sci. Eng. A* **2008**, *476*, 146–156. [CrossRef]

5. Prasad, Y.V.R.K.; Rao, K.P. Effect of homogenization on the hot deformation behavior of cast AZ31 magnesium alloy. *Mater. Design* **2009**, *30*, 3723–3730. [CrossRef]

6. Wei, Z.; Wang, Z.; Zhu, J.; Li, W.; Wang, H. Hot tensile deformation constitutive equation and processing map of AZ61Ce magnesium alloy sheet. *Mater. Res. Express* **2019**, *6*, 046521. [CrossRef]

7. Lou, Y.; Chen, H.; Ke, C.; Long, M. Hot tensile deformation characteristics and processing map of extruded AZ80 Mg Alloys. *J. Mater. Eng. Perform.* **2014**, *23*, 1904–1914. [CrossRef]

8. Xu, Y.; Hu, L.; Sun, Y. Processing map and kinetic analysis for hot deformation of an as-cast AZ91D magnesium alloy. *Mater. Sci. Eng. A* **2013**, *578*, 402–407. [CrossRef]

9. Aliakbari Sani, S.; Ebrahimi, G.R.; Kiani Rashid, A.R. Hot deformation behavior and dynamic recrystallization kinetics of AZ61 and AZ61 + Sr magnesium alloys. *J. Magnes. Alloys* **2016**, *4*, 104–114. [CrossRef]

10. Poliak, E.I.; Jonas, J.J. A one-parmenter approach to determining the critical conditions for the initiation of dynamic recrystallization. *Acta Mater.* **1996**, *44*, 127–136. [CrossRef]

11. Jia, J.; Zhang, K.; Lu, Z. Dynamic globularization kinetics of a powder metallurgy Ti–22Al–25Nb alloy with initial lamellar microstructure during hot compression. *J. Alloys Compd.* **2014**, *617*, 429–436. [CrossRef]

12. Mirzadeh, H.; Najafizadeh, A. Prediction of the critical conditions for initiation of dynamic recrystallization. *Mater. Design* **2010**, *31*, 1174–1179. [CrossRef]

13. Quan, G.; Mao, A.; Luo, G.; Liang, J.; Wu, D.; Zhou, J. Constitutive modeling for the dynamic recrystallization kinetics of as-extruded 3Cr20Ni10W2 heat-resistant alloy based on stress–strain data. *Mater. Design* **2013**, *52*, 98–107. [CrossRef]

14. Sellars, C.M.; Whiteman, J.A. Recrystallization and grain growth in hot rolling. *Met. Sci.* **1979**, *13*, 187–194. [CrossRef]

15. Yu, J.; Zhang, Z.; Xu, P.; Dong, B.; Wang, Q.; Meng, M.; Hao, H.; Li, X.; Yin, X. Dynamic recrystallization behavior of Gd-containing Mg alloy under torsion deformation. *J. Alloys Compd.* **2019**, *787*, 239–253. [CrossRef]

16. Su, Z.; Sun, C.; Fu, M.; Qian, L. Physical-based constitutive model considering the microstructure evolution during hot working of AZ80 magnesium alloy. *Adv. Manuf.* **2019**, *7*, 30–41. [CrossRef]

17. Wei, Z.; Ma, Z.; Wang, Z.; Zhu, J.; Tang, L.; Zheng, W.; Wang, H. Hot tensile deformation mechanism and constitutive equation of AZ61Ce magnesium alloy sheets. *Mater. Res. Express* **2019**, *6*, 116517. [CrossRef]

18. Duan, Y.; Ma, L.; Qi, H.; Li, R.; Li, P. Developed constitutive models, processing maps and microstructural evolution of Pb-Mg-10Al-0.5B alloy. *Mater. Charact.* **2017**, *129*, 353–366. [CrossRef]

19. Hu, D.; Wang, L.; Wang, H. Dynamic Recrystallization Behavior and Processing Map of the 6082 Aluminum Alloy. *Materials* **2020**, *13*, 1042. [CrossRef]

20. Zhou, Z.; Fan, Q.; Xia, Z.; Hao, A.; Yang, W.; Ji, W.; Cao, H. Constitutive Relationship and Hot Processing Maps of Mg-Gd-Y-Nb-Zr Alloy. *J. Mater. Sci. Technol.* **2017**, *33*, 637–644. [CrossRef]

21. Liu, F.; Ma, J.; Peng, L.; Huang, G.; Zhang, W.; Xie, H.; Mi, X. Hot Deformation Behavior and Microstructure Evolution of Cu–Ni–Co–Si Alloys. *Materials* **2020**, *13*, 2042. [CrossRef] [PubMed]

22. Slooff, F.A.; Dzwonczyk, J.S.; Zhou, J.; Duszczyk, J.; Katgerman, L. Hot workability analysis of extruded AZ magnesium alloys with processing maps. *Mater. Sci. Eng. A* **2010**, *527*, 735–744. [CrossRef]

23. Sellars, C.M.; Mc, W.J.; Tegart, G. Relationship between strength and structure in deformation at elevated temperatures. *Mem. Sci. Rev. Met.* **1966**, *63*, 731–745.

24. Chakravartty, J.K.; Prasad, Y.V.R.K.; Asundi, M.K. Processing map for hot working of alpha-zirconium. *Metal. Mater. Trans. A* **1991**, *22*, 829–836. [CrossRef]

25. Tan, Y.; Ma, Y.; Zhao, F. Hot deformation behavior and constitutive modeling of fine grained Inconel 718 superalloy. *J. Alloys Compd.* **2018**, *741*, 85–96. [CrossRef]

26. Sivakesavam, O.; Prasad, Y.V.R. Characteristics of superplasticity domain in the processing map for hot working of as-cast Mg–11.5Li–1.5Al alloy. *Mater. Sci. Eng. A* **2002**, *323*, 270–277. [CrossRef]

27. Chen, Q.; Xia, X.; Yuan, B.; Shu, D.; Zhao, Z.; Han, J. Hot workfability behavior of as-cast Mg–Zn–Y–Zr alloy. *Mater. Sci. Eng. A* **2014**, *593*, 38–47. [CrossRef]

28. Wu, H.; Wu, C.; Yang, J.; Lin, M. Hot workability analysis of AZ61 Mg alloys with processing maps. *Mater. Sci. Eng. A* **2014**, *607*, 261–268. [CrossRef]

29. Lu, J.W.; Yin, D.D.; Ren, L.B.; Quan, G.F. Tensile and compressive deformation behavior of peak-aged cast Mg–11Y–5Gd–2Zn–0.5Zr (wt%) alloy at elevated temperatures. *J. Mater. Sci.* **2016**, *51*, 10464–10477. [CrossRef]

30. Spigarelli, S.; Ruano, O.A.; El Mehtedi, M.; del Valle, J.A. High temperature deformation and microstructural instability in AZ31 magnesium alloy. *Mater. Sci. Eng. A* **2013**, *570*, 135–148. [CrossRef]

31. Liao, C.; Wu, H.; Wu, C.; Zhu, F.; Lee, S. Hot deformation behavior and flow stress modeling of annealed AZ61 Mg alloys. *Prog. Nat. Sci. Mater. Int.* **2014**, *24*, 253–265. [CrossRef]

32. Abbasi-Bani, A.; Zarei-Hanzaki, A.; Pishbin, M.H.; Haghdadi, N. A comparative study on the capability of Johnson-Cook and Arrhenius-type constitutive equations to describe the flow behavior of Mg-6Al-1Zn alloy. *Mech. Mater.* **2014**, *71*, 52–61. [CrossRef]

33. Shamsolhodaei, A.; Zarei-Hanzaki, A.; Ghambari, M.; Moemeni, S. The high temperature flow behavior modeling of NiTi shape memory alloy employing phenomenological and physical based constitutive models: A comparative study. *Intermetallics* **2014**, *53*, 140–149. [CrossRef]

34. Lin, Y.; Xia, Y.; Chen, X.; Chen, M. Constitutive descriptions for hot compressed 2124-T851 aluminum alloy over a wide range of temperature and strain rate. *Comput. Mater. Sci.* **2010**, *50*, 227–233. [CrossRef]

35. Cai, J.; Li, F.; Liu, T.; Chen, B.; He, M. Constitutive equations for elevated temperature flow stress of Ti-6Al-4V alloy considering the effect of strain. *Mater. Des.* **2011**, *32*, 1144–1151. [CrossRef]

36. Lin, Y.; Chen, X. A critical review of experimental results and constitutive descriptions for metals and alloys in hot working. *Mater. Des.* **2011**, *32*, 1733–1759. [CrossRef]

37. Lu, S.; Gu, K.; Zheng, L. *Nonferrous Casting Alloys and Melting*; National Defense Industry Press: Beijing, China, 1983; pp. 173–175.

38. Lin, Y.; Li, L.; Fu, Y.; Jiang, Y. Hot compressive deformation behavior of 7075 Al alloy under elevated temperature. *J. Mater. Sci.* **2011**, *47*, 1306–1318. [CrossRef]

39. Lin, Y.; Li, L.; Jiang, Y. A phenomenological constitutive model for describing thermo-viscoplastic behavior of Al–Zn–Mg–Cu alloy under hot working condition. *Exp. Mech.* **2011**, *52*, 993–1002. [CrossRef]

40. Xu, Y.; Hu, L.; Sun, Y. Deformation behavior and dynamic recrystallization of AZ61 magnesium alloy. *J. Alloys Compd.* **2013**, *580*, 262–269. [CrossRef]

41. Prasad, Y.V.R.K.; Gegel, H.L.; Doraivelu, S.M.; Malas, J.C.; Morgan, J.T.; Lark, K.A.; Barker, D.R. Modeling of dynamic material behavior in hot deformation: Forging of Ti-6242. *Metal. Mater. Trans. A* **1984**, *15*, 1883–1892. [CrossRef]

42. Sarebanzadeh, M.; Mahmudi, R.; Roumina, R. Constitutive analysis and processing map of an extruded Mg–3Gd–1Zn alloy under hot shear deformation. *Mater. Sci. Eng. A* **2015**, *637*, 155–161. [CrossRef]

43. Li, J.; Liu, J.; Cui, Z. Characterization of hot deformation behavior of extruded ZK60 magnesium alloy using 3D processing maps. *Mater. Des.* **2014**, *56*, 889–897. [CrossRef]